axioms

MDPI

Article

On the Kalman Smoother Interpolation Error Distribution in Collocation Comparison of Atmospheric Profiles

Alessandro Fassò [1,*], Hannes Keernik [2,3] and Kalev Rannat [2]

[1] Department of Economics, University of Bergamo, 24127 Bergamo, Italy
[2] Department of Software Science, Tallinn University of Technology, 19086 Tallinn, Estonia; hannes.keernik@taltech.ee (H.K.); kalev.rannat@gmail.com (K.R.)
[3] Department of Bio and Environmental Physics, University of Tartu, 50090 Tartu, Estonia
* Correspondence: alessandro.fasso@unibg.it

Abstract: The intercomparison between different atmospheric monitoring systems is key for instrument calibration and validation. Common cases involve satellites, radiosonde and atmospheric model outputs. Since instruments and/or measures are not perfectly collocated, miss-collocation uncertainty must be considered in related intercomparison uncertainty budgets. This paper is motivated by the comparison of GNSS-RO, the Global Navigation Satellite System Radio Occultation, with ERA5, the version 5 Reanalysis of the European Centre for Medium-range Weather Forecasts. We consider temperature interpolation observed at GNSS-RO pressure levels to the ERA5 levels. We assess the interpolation uncertainty using as 'truth' high-resolution reference data obtained by GRUAN, the Reference Upper-Air Network of the Global Climate Observing System. In this paper, we propose a mathematical representation of the interpolation problem based on the well-known State-space model and the related Kalman filter and smoother. We show that it performs the same (sometimes better) than linear interpolation and, in addition, provides an estimate of the interpolation uncertainty. Moreover, with both techniques, the interpolation error is not Gaussian distributed, and a scaled Student's t distribution with about 4.3 degrees of freedom is an appropriate approximation for various altitudes, latitudes, seasons and times of day. With our data, interpolation uncertainty results larger at the equator, the Mean Absolute Error being $MAE \cong 0.32$ K, and smaller at a high latitude, $MAE \cong 0.21$ K at $-80°$ latitude. At lower altitudes, it is close to the measurement uncertainty, with $MAE < 0.2$ K below the tropopause. Around 300 hPa, it starts increasing and reaches about 0.8 K above 100 hPa, except at the equator, where we observed MAE about 1 K.

Keywords: Kalman smoother; filtering; state-space interpolation; student's t distribution; atmospheric measurement uncertainty; GRUAN data; radiosonde, temperature profiles; collocation uncertainty; GNSS-RO data; ERA5 reanalysis

MSC: 62P12

Citation: Fassò, A.; Keernik, H.; Rannat, K. On the Kalman Smoother Interpolation Error Distribution in Collocation Comparison of Atmospheric Profiles. *Axioms* **2023**, *12*, 902. https://doi.org/10.3390/axioms12100902

Academic Editor: Elisa Varini

Received: 5 July 2023
Revised: 12 September 2023
Accepted: 19 September 2023
Published: 22 September 2023

1. Introduction

Currently, along with atmospheric parameters measured at a fixed point in space, an array of meteorological quantities (e.g., wind speed and direction, temperature, pressure, humidity, atmospheric composition) are acquired as vertical profiles describing the physical properties of a column of air varying with altitude. This is made possible by major technological advances over the past few decades regarding atmospheric sensors and sensor platforms. In high-resolution (≈1 m) applications, traditional instruments such as tethersondes, radiosondes and dropsondes are used for vertical profiling [1]. However, to a certain extent (although at relatively coarse vertical resolution), these in-situ measurements can be complemented with different remote sensing techniques using ground-based instruments (e.g., lidars and microwave radiometers) and satellite-born instruments.

Investigating the vertical structure of the atmosphere with satellite instruments dates from the 1970s [2]. The first publications on intercomparisons of satellite and radiosonde profiles proved the capability of the new technique [3–6], which has largely compensated for the limitations in coverage over land and oceans inherent in balloon-born measurements [7]. Most notably, the datasets of temperature, humidity and pressure, available through Global Navigation Satellite System Radio Occultations (GNSS-RO) [8–10] since the early 2000s and serving as the main input for numerical weather predictions (NWPs), are reliable data sources supporting climate change assessments [11].

Although having a relatively coarse horizontal resolution (∼300−400 km), the effective vertical resolution of GNSS-RO measurements below 15-km altitudes is from 100 m to 300 m [12], which is suitable for resolving relatively small-scale atmospheric variability in vertical dimensions [13–15]. In addition, hyperspectral infrared sounders, such as the Atmospheric Infrared Sounder (AIRS) onboard NASA's Aqua satellite and the Infrared Atmospheric Sounding Interferometers (IASIs) on the EUMETSAT MetOp satellites, have become valuable data sources for a wide range of applications [16–18]. Although having some known limitations [13,19–23], GNSS-RO, AIRS and IASI measurements are now assimilated into operational NWP models and different reanalyses, which allows for the investigation of the state of the atmosphere in a three-dimensional grid of points [11]. Whether an operative NWP or a reanalysis, the final product is a gridded representation of a geophysical quantity based on irregularly spaced observations. For example, the reanalysis of the European Centre for Medium-range Weather Forecasts (ERA5) provides hourly fields available at a horizontal resolution of 31 km on 37 pressure levels, from the surface up to 1 hPa [24,25]. According to the standard atmosphere, the vertical resolution of ERA5 is <250 m at the lowest levels and up to 1 km at tropopause height.

1.1. Background on Intercomparisons

With the diversity of atmospheric sounding techniques, new challenges arise for establishing reference methods. This, in turn, requires the assessment of instrumental performance and the quantification of biases and uncertainties. Such extensive knowledge is derived from laboratory tests and intercomparisons, the latter being a common practice and a requirement for improving the global climate observation system [26–28]. An intercomparison aims to determine whether different observing systems agree within their known limitations [29].

Comparisons of atmospheric profiles derived from two or more instruments must consider the spatial displacement of the measurements. Generally, the instruments included in the analysis are relatively close to each other but usually not measured at the same point in space and time (not the case for twin radiosoundings, where different instruments are fixed to the same ascending balloon). Typically, an assumption is made that within a few hours and some tens of kilometres in horizontal displacement, the properties of the atmosphere do not vary significantly, allowing for the comparison of two ground-based soundings within these limits without any horizontal and/or temporal interpolation [30]. However, the criteria for comparing ground-based sounding with a satellite-born counterpart are less strict to increase the number of satellite profiles suitable for collocation, the latter directly depending on the position(s) of the satellite(s). The horizontal and temporal mismatch limits, used in earlier publications, reach up to several hundreds of kilometres and seven hours, respectively [31–37].

On the other hand, a vertical mismatch of the levels used in collocated profiles is often addressed through interpolation of a profile with a higher vertical resolution (e.g., radiosonde) to the pressure levels of another profile with a lower resolution (e.g., satellite product). For example, the GNSS-RO observations are defined along a vertical grid (60 levels in the case of GNSS-RO products [31,38]), which does not coincide with the irregular grid of the in-situ profiles (several thousand in the case of raw radiosonde data). Therefore, the radiosonde collocated profiles are usually interpolated to the vertical levels of the GNSS-RO. Similar interpolation is inevitable while comparing instruments with

NWP models. For example, the IASI temperatures are given at 90 pressure levels (version 4 and 5 temperature profiles) or at 101 pressure levels (version 6 temperature profiles). To compare the profiles with ERA5, the IASI temperature profiles are interpolated to the ERA5 pressure levels [18]. This step introduces an interpolation uncertainty component that must be considered in the total collocation uncertainty budget, including instrumental uncertainty and components from horizontal and temporal mismatches [39].

As a common practice in climate research, it is customary to evaluate the agreement between diverse methodologies that yield time series data for Essential Climate Variables (ECVs). The presence of ECVs and their associated uncertainties are indispensable for determining whether two instruments (or techniques) stationed at the same location are measuring identical phenomena (i.e., whether their time series exhibit statistical concordance). The procedure elucidating the metrological closure, which involves assessing the statistical concordance of distinct measurements while factoring in the total collocation uncertainty budget, is outlined in [26].

It must be noted that intercomparisons can also be carried out between different numerical models [40,41] and radiosonde types [42,43], between an instrument and any other type of instruments suitable for measuring the same parameters in the same atmospheric conditions [44]. In the case of intercomparisons that include a three-dimensional model, an additional horizontal interpolation of model data to the locations of the data points from the instrument is applied [18,41].

1.2. Motivation and Novelty

This article is motivated by a comparison of GNSS-RO temperatures with ERA5 outputs. We observe that both GNSS-RO retrievals and ERA5 model outputs are spatially and temporally smoothed, as discussed previously. Hence, to separate interpolation uncertainty from the other collocation uncertainty sources, we consider reference measurements at ERA5 levels with high quality and high resolution. In fact, we use as 'truth' data obtained by GRUAN, i.e., the Reference Upper-Air Network of the Global Climate Observing System (https://www.gruan.org/, accessed on 13 March 2023). In particular, we use reference measurements given by GRUAN Data Processing (GDP) for Vaisala RS41 radiosonde [45], which are available at both the GNSS-RO and ERA5 pressure levels, with a 1-s accuracy.

We provide a novel interpolation algorithm based on the well-known state-space representation and the Kalman filter (e.g., [46]). It is shown to have a performance equivalent to linear interpolation, but it also provides an estimate of the interpolation uncertainty. The new algorithm and linear interpolation are tested in interpolating the 37 ERA5 pressure levels starting from the 60 GNSS-RO levels. We compare the interpolated values with the true ones and assess the related interpolation uncertainty by latitude, altitude, season and time of day.

An important by-product is the study of the interpolation error distribution, which is shown to be non-Gaussian. A scaled Student's t distribution adapts well to our data. Due to this result, using coverage factors $k = 2$ or 3 in Immler's inequality [26] is questioned, and an alternative is provided.

Previous literature on interpolation uncertainty [47,48] considered the case of missing data interpolation for radiosonde temperature and humidity based on Gaussian Process (GP) interpolation in the frame of GRUAN Data Processing [49]. The main difference is that these two papers considered high-resolution data, while here, the temporal gaps among data are much larger. For this reason, various preliminary attempts to use GP interpolation were not successful, and we turned to the current state-space model approach.

1.3. Paper Structure

The rest of the paper is organised as follows. Section 2.1 introduces the GNSS-RO and GRUAN data used in the rest of the paper. Section 2.2 explains the state-space model proposed for interpolation, and short Section 2.3 defines the interpolation error and its empirical uncertainty. Section 2.4 addresses the concept of statistical concordance between

measurements and the shape of the error distribution, and Section 2.5 explains how to handle the Student's t distribution estimation. Section 3 presents the uncertainty results by station, altitude, season and time of day. Section 4 provides a discussion of the obtained results, and Section 5 draws some general conclusions.

2. Materials and Methods

2.1. Data

The current analysis considers collocated, GRUAN-processed radiosonde (RS41-GDP1, [49,50]) and GNSS-RO measurements from the Metop satellite collected during 2020. The Metop atmospheric profile data were obtained from the publicly available archive of the Radio Occultation Meteorology Satellite Application Facility (ROM SAF, see the Data Availability Statement below). A horizontal distance of 300 km and a time difference of 3 h are used as collocation criteria. The data are categorised by time of day based on the solar elevation angle (SEA), which depends on time, latitude and longitude. The SEA ranges for 'day', 'night' and 'dusk/dawn' data were 7.5 to 90, −90 to −7.5 and −7.5 to 7.5 degrees, respectively. The season was determined based on the latitude and the month to consider the seasonal differences between the southern and northern hemispheres. The data included in this study are summarised in Table 1.

Table 1. GRUAN stations and counts for the data used. Columns ERA5 and GNSS-RO report the number of available measurements at the corresponding pressure levels. GNSS-RO are used for learning, while ERA5 are used for testing.

Station	Latitude	Longitude	ERA5	GNSS-RO	Profiles
Lauder	−45.05°	169.68°	9750	14,790	328
Lindenberg	52.21°	14.12°	11,104	16,564	374
Ny-Alesund	78.92°	11.93°	6002	9040	202
Ross Island	−77.85°	166.65°	4378	6777	174
Singapore	1.30°	103.80°	2829	4100	94
Overall			34,063	51,271	1172

The data set is seasonally balanced for all stations but Ross Island, which has in summer and fall approximately one-half of the observations in winter and spring (see Table 2). Considering the time of day, some stations are strongly unbalanced with only two or three profiles in dusk/dawn or night (see Table 3). This will be considered in the subsequent analysis.

Table 2. Number of profiles of GRUAN stations by season.

Station	Spring	Summer	Autumn	Winter
Lauder	91	74	84	79
Lindenberg	107	82	91	94
Ny-Alesund	75	36	30	61
Ross Island	57	66	23	28
Singapore	28	19	28	19
Overall	358	277	256	281

Table 3. Number of profiles of GRUAN stations by time of day.

Station	Day	Dusk/Dawn	Night
Lauder	163	3	162
Lindenberg	197	49	128
Ny-Alesund	81	54	67
Ross Island	98	40	36
Singapore	32	60	2
Overall	571	206	395

2.2. Interpolation by State-Space Models

In this section, we introduce a statistical model based on the well-known class of state-space models [46], propagating the measurement uncertainty to interpolated points while taking into account interpolation uncertainty.

Let y_i denote the observation of the geophysical quantity of interest, e.g., temperature [K], at pressure level p_i, $i = 1, ..., n$ where n is the number of observations of the profile under consideration. We assume a measurement equation error for y_i given by

$$y_i = x_i + \varepsilon_i. \tag{1}$$

Here, x_i is the 'true' state, and ε_i is the random measurement error with uncertainty $u_i = \sqrt{Var(\varepsilon_i)}$, where $Var()$ is the variance operator. For the state x, we assume locally linear dynamics with respect to pressure, given by

$$x_i = x_{i-1} + \alpha_i(p_i - p_{i-1}) + \eta_{x,i} \tag{2}$$

$$\alpha_i = \alpha_{i-1} + \eta_{\alpha,i} \tag{3}$$

where $\eta_{x,i}$ and $\eta_{\alpha,i}$ are independent innovation processes with zero mean and variance σ_x^2 and σ_α^2, respectively. Equation (2) states that apart from the stochastic component $\eta_{x,i}$, the geophysical state has a local linear variation with respect to the pressure levels. Equation (3) implies a smooth variation of the coefficient α.

For any pressure level $p^* \in [p_i, p_{i-1}]$ the optimal estimate of the corresponding state x^* is given by the following conditional expectation

$$\hat{x}^* = E(x^*|y_1, \ldots, y_n) \tag{4}$$

which is readily computed by the Kalman smoother (KS) algorithm under Gaussian assumptions. In addition, the uncertainty at p^* is given by

$$u_{KS}(\hat{x}^*)^2 = Var(x^*|y_1, \ldots, y_n) \tag{5}$$

which also is an output of the above-mentioned KS algorithm.

2.3. Interpolation Errors and Uncertainty

For each single profile, let us denote by (y_i, p_i), $i = 1, \ldots, n$ the observations at GNSS-RO levels, and by (x_j^*, p_j^*), $i = 1, \ldots, n^*$ the true values at ERA5 levels. Let $\tilde{y}_j^*$ be the linear interpolation at ERA5 level p_j^*, and let $e_{LINT,j} = \tilde{y}_j^* - x_j^*$ be the corresponding interpolation error. Moreover, let $\hat{x}_j^*$ be the KS interpolation given in Equation (4) at ERA5 level p_j^*, and let $e_{KS,j} = \hat{x}_j^* - x_j^*$ be the corresponding error.

In the sequel, we focus on altitudes below 10 hPa. As a result, we have $n^* = 31$ ERA5 levels and $n \leq 46$ GNSS-RO levels. The latter depends on missing data, and, on average, we have $n = 44$.

'Observed' interpolation uncertainty is computed using root mean square error (RMSE) and mean absolute error (MAE). Let GNSS-RO profiles be indexed by $id = 1, ..., N = 1172$ as in Table 1, and consider a subset $\mathcal{S}$ of all profiles, e.g., a station or a season. Of course, the

number of elements of $\mathcal{S}$ cannot exceed N, namely $||\mathcal{S}|| \leq N$. For methods $m = LINT, KS$, we have

$$RMSE_{m,\mathcal{S}} = \sqrt{\frac{1}{n^*||\mathcal{S}||} \sum_{j \leq n^*, id \in \mathcal{S}} e^2_{m,id,j}}$$

and

$$MAE_{m,\mathcal{S}} = \sqrt{\frac{1}{n^*||\mathcal{S}||} \sum_{j \leq n^*, id \in \mathcal{S}} ||e_{m,id,j}||}.$$

It is well known that RMSE, being a quadratic metric, is suited for Gaussian errors but is prone to outliers and high tails. Instead, MAE is a robust metric suitable for outlier resistance and high tails.

2.4. Non-Gaussian Errors

In collocation comparisons literature [26], two generic measurements m_1 and m_2, with uncertainties u_1 and u_2, are said to be in statistical concordance or in agreement if the error, $e = m_1 - m_2$, is small, namely

$$|e| < k \cdot u_e \tag{6}$$

for $k = 2$. In this formula, u_e is the collocation uncertainty. If the uncertainties are uncorrelated and no collocation mismatch affects the measurements, then $u_e = \sqrt{u_1^2 + u_2^2}$. It is well known that $k = 2(3)$ has the interpretation of a statistical test with false rejection probability $\alpha \cong 5\%(0.27\%)$ if e is Gaussian distributed.

If the error distribution has higher tails than the Gaussian distribution, the interpretation of k may be different. If the error has a scaled Student's t distribution, with $\nu > 4$ degrees of freedom and scale parameter $u_e = \sqrt{var(e)}$, then k in Equation (6) is related to a standardized Student's t distribution. That is a distribution with variance one. From Table 4, we see that its 97.5% percentile is close to the corresponding Gaussian percentile, namely 1.96, for any $\nu > 4$. Instead, the probability of large errors, related to $k \geq 3$, for the standardized t distribution is much larger than the Gaussian counterpart, even if the two measurements come from the same instrument. See the examples in Table 4.

Table 4. k-Values of Equation (6) based on standardized Student's t distribution for $\alpha = 0.05$ and 0.0027, and tail probabilities for various degrees of freedom ν compared to the Gaussian case. Note that the first two columns are obtained by the usual Student's t quantiles after multiplying by $\sqrt{\frac{\nu}{\nu-2}}$. Similarly, the tail probabilities in the last two columns are obtained by the thresholds 3 and 4 rescaled with the same factor.

ν	$\alpha = 0.05$	$\alpha = 0.0027$	P(|t|>3)	P(|t|>4)
4	1.96	4.68	1.32×10^{-2}	4.80×10^{-3}
5	1.99	4.27	1.17×10^{-2}	3.59×10^{-3}
10	1.99	3.54	7.30×10^{-3}	1.19×10^{-3}
20	1.98	3.25	4.90×10^{-3}	4.00×10^{-4}
300	1.96	3.02	2.8×10^{-3}	1.00×10^{-4}
Gaussian	1.96	3.00	2.70×10^{-3}	1.00×10^{-4}

2.5. Inference for the Student's t Distribution

In our case study, both linear interpolation and KS errors have kurtosis, $kurt(e) \cong 20$, well above the Gaussian value of three. The top panel of Figure 1 clearly shows the big departure from the normal distribution, and any test of normality would reject this hypothesis. In fact, the KS error distribution, shown in Figure 2, is very peaky and has very high tails that may be reasonably approximated by a Student's t with few degrees of freedom, as shown in the bottom panel of Figure 1. We tested the null of scaled Student's t distribution using the Kolmogorov-Smirnov test. Partly due to the large sample size, the relatively small departure of the empirical tails from the nominal one shown in Figure 1,

bottom panel, led to rejection at usual significance levels. Hence, we interpret the Student's t distribution as an approximation which improves on the Gaussian assumption.

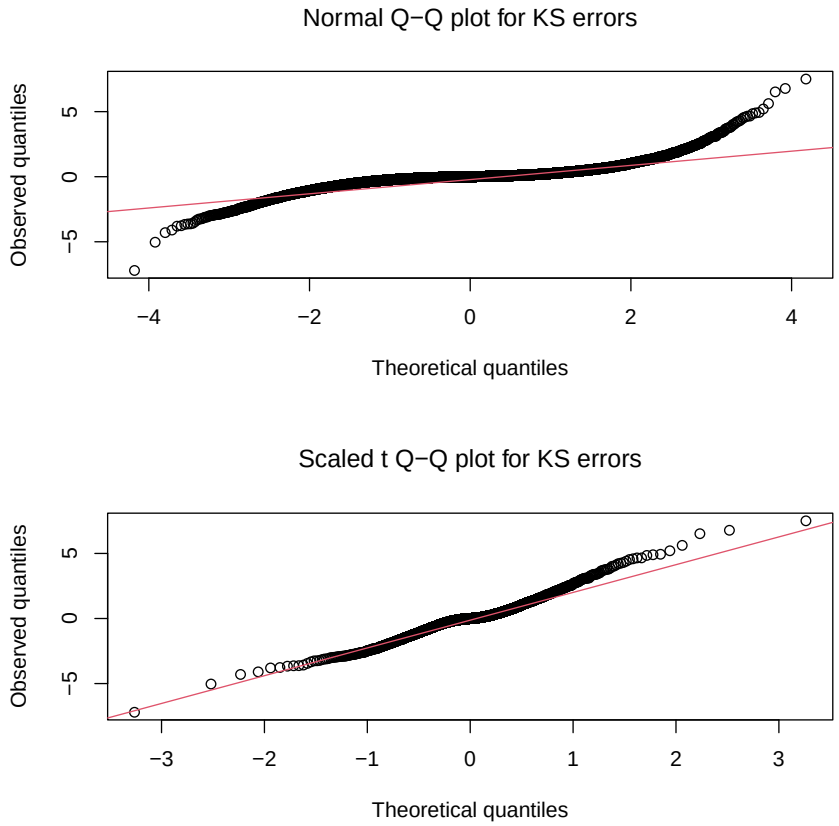

Figure 1. QQ-plots of KS errors at ERA5 levels. Top panel: Normal distribution; Bottom panel: Scaled Student's t distribution with $\nu = 4.3$ degrees of freedom.

It is interesting to note that the Student's t distribution may be seen as the compound of the Gaussian distribution with variance given by an inverse Gamma random variable. This evidence could bring us to extend the Gaussian state-space model of Section 2.2. Recently, Kalman filters have been developed using the Student's t distribution for the measurement error in Equation (1); see, e.g., [51]. In our case, we have a sampling issue since, apart from the testing case on GRUAN data, we do not have available measurements for ERA5 levels. As a result, the RMSE for ERA5 levels is much larger than for GNSS-RO levels.

For this reason, we postpone the full non-Gaussian state-space model for future research. Instead, in this paper, we use a two-step approach. First, we compute linear and (Gaussian) KS interpolation. Second, we fit the errors by a scaled t distribution with a degrees of freedom parameter ν and standard error σ, depending on the data. This approach allows us better to understand the uncertainty of the data at hand.

In particular, the $\nu > 4$ parameter is estimated by the method of moments,

$$\hat{\nu} = 4 + \frac{6}{kurt(e) - 3}. \tag{7}$$

Then, the σ scale parameter is estimated by the plug-in maximum likelihood method, $\hat{\sigma} = \hat{\sigma}_{\hat{\nu}}$. Since the sample sizes are large, we are not concerned about the loss in efficiency related to the method of moments.

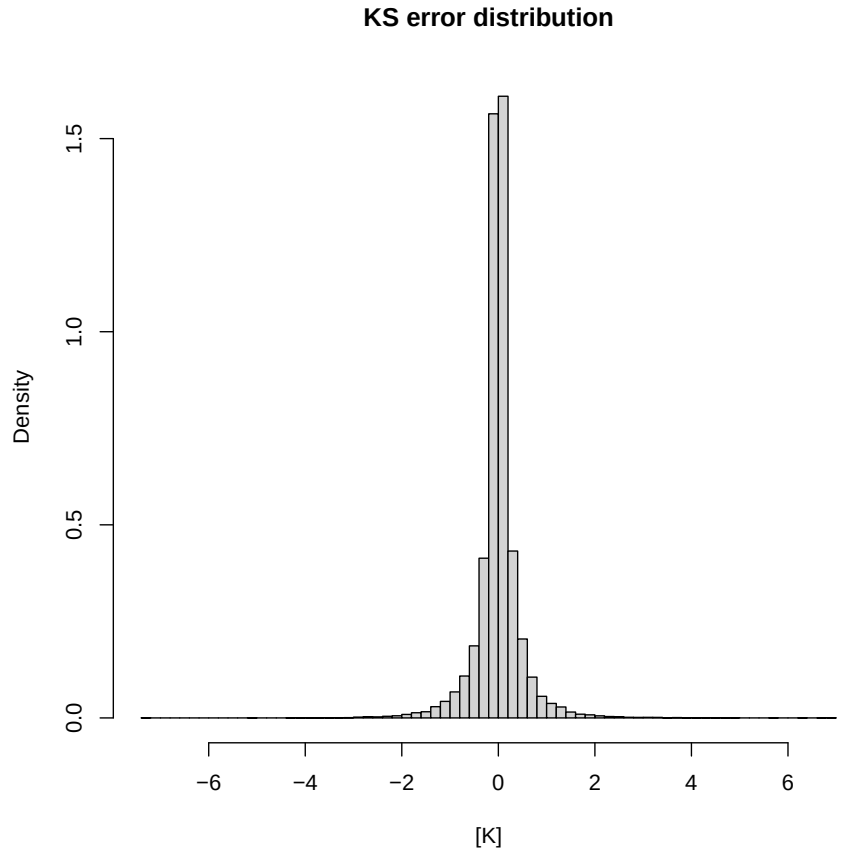

Figure 2. Frequency distribution of KS errors at ERA5 levels.

3. Results

Using the data from Table 1 and the methods detailed in the previous section, we computed linear and KS interpolation and the related errors e_L and e_K at ERA5 levels. The first important result is that the errors obtained by the two methods are equivalent. In fact, the mean difference is quite small, $\overline{e_L - e_K} = 0.004\ K$, the Spearman correlation coefficient is quite large $r(e_L, e_K) > 0.95$ and $RMSE(e_L - e_K) = 0.14\ K$. Hence in the sequel, we focus on KS results and omit the subscript K wherever it is clear.

In this section, we assess the interpolation uncertainty by latitude, altitude, season and time of day. In particular, we consider the RMSE, which, for different reasons, may be prone to outliers and non-Gaussianity. Additionally, we consider the robust metrics given by MAE and Student's t scale, σ.

3.1. Uncertainty by Station

Since the GRUAN stations used are located on various continents and at latitudes spanning from +78° to −78°, an important question is related to the geographical stability of the interpolation uncertainty.

Table 5 reports various uncertainty measures by station. As a reference, we give the median of the measurement uncertainty reported by the GDP and the interpolation uncertainty given by KS. We also report the RMSE, MAE, Student's t scale and degrees of freedom parameters for the KS interpolation errors. The standard errors of these uncertainty measures and t-distribution parameters are very small, as shown in Table 6.

It may be observed from the last column of Table 5 that the tail parameter $\hat{\nu}$ is essentially constant along the stations. Considering interpolation uncertainty, the tropic station of Singapore has the highest values for the three metrics considered. For example, the Median KS uncertainty is more than twice the overall value. This is not due to measurement uncertainty. In fact, Singapore's median measurement uncertainty is very close to the overall value. The antarctic station of Ross Island has the lowest metrics even if the GDP

uncertainty is higher. The northern stations have similar interpolation metrics, even if Lindenberg has a considerably lower GDP uncertainty.

Table 5. KS uncertainty [K] by station. Column details: $MED(u)$, Median measurement uncertainty; $MED(u_{KS})$, Median KS interpolation uncertainty; $RMSE_{KS}$, Root mean square interpolation error at ERA5 levels; MAE_{KS}, Mean absolute interpolation error; $\hat{\sigma}$, Maximum t-likelihood scale estimate; $\hat{\nu}$, Moment estimate of degrees of freedom given by Equation (7).

Station	$MED(u)$	$MED(u_{KS})$	$RMSE_{KS}$	MAE_{KS}	$\hat{\sigma}$	$\hat{\nu}$
Lauder	0.246	0.384	0.498	0.284	0.270	4.392
Lindenberg	0.118	0.374	0.456	0.257	0.243	4.352
Ny-Alesund	0.216	0.379	0.423	0.245	0.235	4.421
Ross Island	0.257	0.268	0.341	0.211	0.209	4.526
Singapore	0.247	0.747	0.702	0.321	0.243	4.334
Overall	0.240	0.369	0.476	0.262	0.242	4.307

Table 6. Standard errors of KS uncertainty [K] by station. Column details: see Table 5.

	Standard Errors			
Station	$RMSE_{KS}$	MAE_{KS}	$\hat{\sigma}$	$\hat{\nu}$
Lauder	0.004	0.004	0.003	0.105
Lindenberg	0.003	0.004	0.002	0.137
Ny-Alesund	0.004	0.004	0.003	0.081
Ross Island	0.004	0.004	0.003	0.102
Singapore	0.009	0.012	0.005	0.044
Overall	0.002	0.002	0.001	0.037

From these figures, it can be observed that the interpolation uncertainty is more influenced by atmospheric dynamics than measurement uncertainty. It is also interesting to observe the overestimation of the uncertainty provided by the RMSE due to its sensitivity to large errors. Once the high tails are taken into account using the t-distribution approach, the maximum likelihood estimate of the uncertainty, namely $\hat{\sigma}$, is noticeably smaller than RMSE and close to the robust metric given by MAE.

3.2. Uncertainty by Altitude

Figure 3 depicts the vertical behaviour of interpolation uncertainty assessed by MAE and compared to the median of measurement uncertainty, u, and KS uncertainty, u_{KS}, as in Equation (5). Similarly, Figure 4 describes the RMSE behaviour and compares it to the quadratic means of u and u_{KS}.

It may be noted that both MAE and RMSE interpolation uncertainties are close to the measurement uncertainty below the tropopause, with $MAE < 0.2$ K. Instead, around 300 hPa, both show an increase and an even steeper increase above that, with MAE near 0.8 and K above 100 hPa. Additional insight is provided by Figure 5, which depicts the vertical profile of MAE by station. It is clearly seen that the equatorial station of Singapore has the larger uncertainty in the upper atmosphere. After excluding this, the other stations are in line with the above uncertainty limit of 0.8 K above 250 hPa. In particular, the antarctic station of Ross Island has the smallest interpolation uncertainty in the upper atmosphere.

It is interesting to note that the interpolation uncertainty may be smaller than the measurement uncertainty. This is consistent with the fact that the temperature profile may be very smooth, and using neighbouring observations may improve the measurement precision. Comparing the blue and green lines of Figures 3 and 4, we observe that KS and LINT are quite similar, but, at the tropopause, near 300 hPa, KS provides better interpolation.

The KS interpolation uncertainty (u_{KS}) is larger than RMSE and/or MAE below 200 hPa and smaller above this level. For operational use of u_{KS}, we suggest the correction given by Equation (15) of [47].

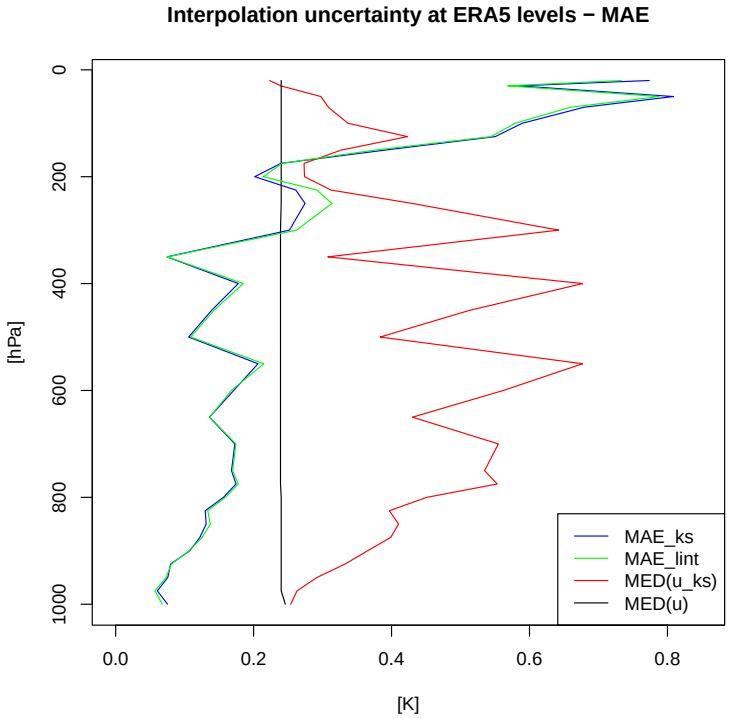

Figure 3. Robust uncertainty profiles. The blue line is the MAE of the KS interpolation; the green line is the MAE of the linear interpolation; the red line is the median of the KS uncertainty; the black line is the median of GDP measurement uncertainty.

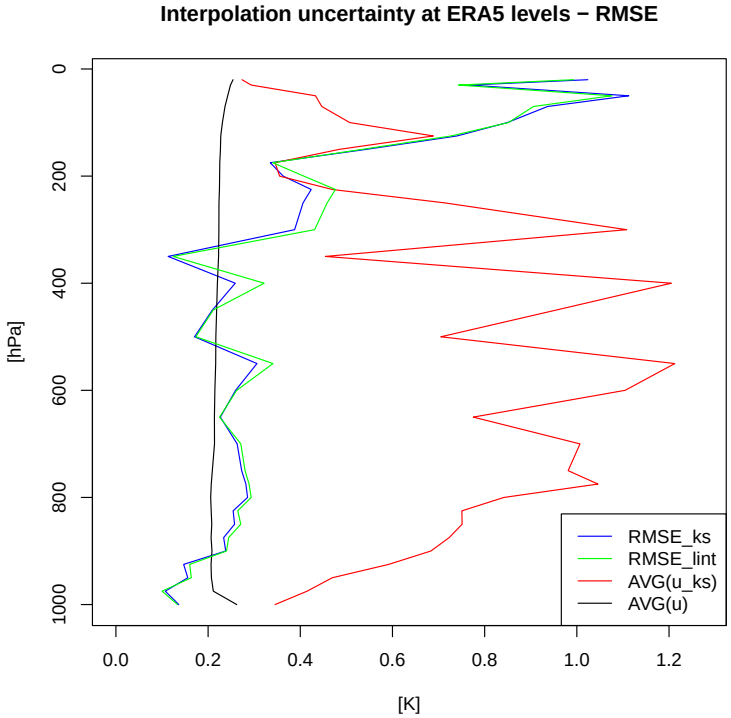

Figure 4. RMSE uncertainty profiles. The blue line is the RMSE of the KS interpolation; the green line is the mean square error of the linear interpolation; the red line is the quadratic mean of KS uncertainty; the black line is the quadratic mean of GDP measurement uncertainty.

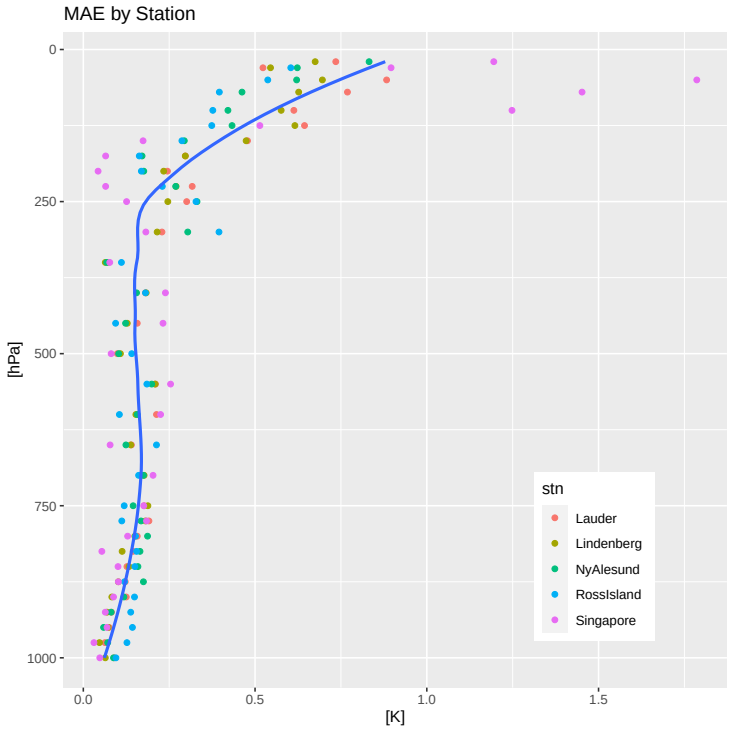

Figure 5. MAE profile by station. Station colours are explained in the panel's graphic legend. The blue curve is the station average.

3.3. Uncertainty by Season

After observing the uncertainty sensitivity to latitude in Section 3.1, we tested for similar seasonal effects as reported in this section. Reading Table 7 from right to left and considering the related standard errors reported in Table 8, we observe that the t-distribution parameters ν and σ are quite close for the different seasons. The minimum interpolation uncertainty (either RMSE, MAE or σ) is observed in summer with a difference of $0.01-0.02$ K with respect to the overall quantity. Again, we have little uncertainty variation between seasons.

Table 7. KS uncertainty [K] by season. Column details: see Table 5.

Season	Profiles	$MED(u)$	$MED(u_{KS})$	$RMSE_{KS}$	MAE_{KS}	$\hat{\sigma}$	$\hat{\nu}$
Spring	358	0.24	0.384	0.486	0.262	0.238	4.292
Summer	277	0.247	0.340	0.459	0.251	0.232	4.268
Autumn	256	0.239	0.357	0.479	0.272	0.258	4.494
Winter	281	0.215	0.404	0.477	0.264	0.245	4.267
Overall	1172	0.240	0.369	0.476	0.262	0.242	4.307

Table 8. Standard errors of KS uncertainty [K] by season. Column details: see Table 5.

		Standard Errors			
Season	**Profiles**	$RMSE_{KS}$	MAE_{KS}	$\hat{\sigma}$	$\hat{\nu}$
Spring	358	0.003	0.004	0.002	0.064
Summer	277	0.004	0.004	0.003	0.102
Autumn	256	0.004	0.005	0.003	0.070
Winter	281	0.004	0.004	0.003	0.062
Overall	1172	0.002	0.002	0.001	0.037

3.4. Uncertainty by Time of Day

Tables 9 and 10 report the interpolation uncertainty metrics and their standard errors classified by time of day for the entire data set and for the Lindenberg data alone. It is seen that during dusk/dawn, the overall interpolation error distribution has higher tails, with lower degrees of freedom ν and a higher RMSE, exceeding by about 0.03 K the day and night times. This is not the case for Lindenberg data. To have further insight, Tables 11 and 12 provide MAE and RMSE by station and time of day. It is again clear that the variation of uncertainty is led more by geography than by time of day. Notice that Singapore shows a reduction in the nighttime, but the standard error is higher due to the small profile number for this case, as mentioned in Section 2.1 and highlighted in Table 3.

Table 9. KS uncertainty [K] by time of day for the overall data set and for Lindenberg data. Column details: see Table 5.

Time of Day	Profiles	$MED(u)$	$MED(u_{KS})$	$RMSE_{KS}$	MAE_{KS}	$\hat{\sigma}$	$\hat{\nu}$
			Overall				
Day	571	0.252	0.342	0.469	0.259	0.241	4.300
Dusk/dawn	206	0.240	0.432	0.510	0.261	0.228	4.277
Night	395	0.239	0.396	0.467	0.266	0.251	4.356
			Lindenberg				
Day	197	0.153	0.334	0.438	0.254	0.252	4.729
Dusk/dawn	49	0.094	0.409	0.436	0.248	0.241	4.678
Night	128	0.081	0.448	0.490	0.266	0.243	4.221

Table 10. Standard errors of KS uncertainty [K] by season. Column details: see Table 5.

		Standard Errors			
Time of Day	Profiles	$RMSE_{KS}$	MAE_{KS}	$\hat{\sigma}$	$\hat{\nu}$
		Overall			
Day	571	0.003	0.003	0.002	0.057
Dusk/dawn	206	0.005	0.006	0.003	0.048
Night	395	0.003	0.004	0.002	0.120
		Lindenberg			
Day	197	0.004	0.005	0.003	0.071
Dusk/dawn	49	0.008	0.009	0.007	0.091
Night	128	0.006	0.007	0.004	0.127

Table 11. MAE and its standard errors of KS uncertainty [K] by station and time of day. Column details: see Table 5.

	MAE_{KS}			Standard Errors		
	Day	Dusk/Dawn	Night	Day	Dusk/Dawn	Night
Lauder	0.283	0.282	0.284	0.006	0.036	0.006
Lindenberg	0.254	0.248	0.266	0.005	0.009	0.007
Ny-Alesund	0.257	0.236	0.239	0.007	0.008	0.007
Ross Island	0.202	0.222	0.223	0.005	0.009	0.009
Singapore	0.333	0.316	0.281	0.021	0.014	0.063

Table 12. RMSE and its standard errors of KS uncertainty [K] by station and time of day. Column details: see Table 5.

	$RMSE_{KS}$			Standard Errors		
	Day	**Dusk/Dawn**	**Night**	**Day**	**Dusk/Dawn**	**Night**
Lauder	0.507	0.444	0.489	0.005	0.033	0.005
Lindenberg	0.438	0.436	0.490	0.004	0.008	0.006
Ny-Alesund	0.444	0.411	0.406	0.006	0.007	0.006
Ross Island	0.337	0.353	0.336	0.005	0.008	0.008
Singapore	0.733	0.690	0.557	0.017	0.011	0.051

4. Discussion

The interpolation of temperature at ERA5 levels using data on GNSS-RO levels results in error distributions with tails higher than the Gaussian distribution. The analysis based on GRUAN-processed radiosonde data shows that, in general, a t-distribution with about $\nu = 4.3$ degrees of freedom is an appropriate approximation. We suggest using MAE and/or Student's t σ parameter to assess such a non-Gaussian uncertainty. Comparing them to RMSE helps to highlight the high tail's impact on uncertainty.

The overall uncertainty of the temperature profiles was about 0.25 K for MAE and t-distribution scale parameter σ. It was about 0.5 K for RMSE. Such figures are mainly influenced by latitude and geography, with higher values in the tropics and smaller ones near the poles. In particular, the Ross Island station at $-78°$ latitude gives uncertainties that are smaller than the Ny-Alesund station at +78° latitude. This effect is more evident in higher atmospheres, above 300 hPa, where MAE increases up to 0.8 K for most stations, except for the equatorial station of Singapore, where a discernible increase in the degree of interpolation uncertainty within the upper troposphere/lower stratosphere was revealed, exceeding 1 K. By contrast, Ross Island has the smallest uncertainty at these altitudes. The findings regarding temperature uncertainty dependence on latitude are consistent with previous research that has observed a pronounced change in temperature lapse rate within the specified altitude range in the tropics [20]. When the lapse rate undergoes rapid changes with altitude, it becomes increasingly difficult to estimate temperatures accurately through interpolation. In such cases, larger interpolation errors become inevitable.

It may be noted that the horizontal and vertical variations dominate the temporal sources of variation considered, namely season and time of day, which can be ignored in this respect.

We considered both linear interpolation and interpolation based on Kalman smoother. The two methods produced results that were very close in terms of performance, but Kalman smoother was slightly better near the tropopause. In addition, Kalman smoother provided interpolation uncertainties for individual profiles, which may be useful in practice. Interstingly, the Kalman smoother interpolation uncertainty was often smaller than the measurement uncertainty. This is due to the smoothness of the temperature profiles, so using neighbouring information improves the understanding of the temperature state.

5. Conclusions

Two important take-home messages were raised from this study. The first one is related to collocation uncertainty. In fact, the methodology outlined in this paper represents an initial step towards establishing the statistical agreement between two independent methods that measure temperature with different vertical resolutions. In particular, thanks to the assessment of interpolation uncertainty developed here, future research on the comparison of GNSS-RO temperatures with ERA5 outputs will be able to define a detailed uncertainty budget where the interpolation component may be extracted.

The second one is more general and calls for a rethinking of Immler's inequality. Usually, the measurement error is taken as Gaussian distributed. This paper provides evidence that, at least in comparisons with vertical miss-collocation, this may not be true.

In such a case, high-tail distributions need to be used. An interesting point of this paper is that, at least for the data used, the height of the error distribution tails does not depend on latitude, altitude, season or time of day. It behaves like a constant of the problem, and further studies will be able to deepen this result and its generality.

Author Contributions: Conceptualisation, A.F., H.K. and K.R.; methodology, A.F.; software, A.F. and H.K.; validation, A.F.; data analysis, A.F. and H.K.; statistical modelling, A.F.; data curation, H.K.; writing—original draft preparation, A.F., H.K. and K.R.; writing—review and editing, A.F., H.K. and K.R.; visualisation, A.F. All authors have read and agreed to the published version of the manuscript.

Funding: This research was funded by Estonian Research Council team grant PRG1726.

Data Availability Statement: GRUAN data are available at https://www.gruan.org/data/file-archive/rs41-gdp1-at-lc accessed on 13 March 2023; registration is required for downloading the data sets. GNSS-RO measurements from the Metop satellite can be obtained from the publicly available archives of the Radio Occultation Meteorology Satellite Application Facility [38]; registration is required for downloading the data sets.

Acknowledgments: We wish to express our sincere thanks to the GRUAN Lead Centre and especially to Michael Sommer for their help and guidance in obtaining data and in the release interpretation. H.K. acknowledges the support from the Estonian Research Council team grant PRG1726.

Conflicts of Interest: The authors declare no conflict of interest.

References

1. Tropea, C.; Yarin, A.L.; Foss, J.F. *Springer Handbook of Experimental Fluid Mechanics*; Springer: Berlin/Heidelberg, Germany, 2007; Volume 1.
2. Thompson, O.E.; Eom, J.K.; Wagenhofer, J.R. On the resolution of temperature profile finestructure by the NOAA satellite vertical temperature profile radiometer. *Mon. Weather. Rev.* **1976**, *104*, 117–126. [CrossRef]
3. Smith, W.L.; Woolf, H. *An Intercomparison of Meteorological Parameters Derived from Radiosonde and Satellite Vertical Temperature Cross Sections*; National Environmental Satellite Service: Silver Spring, MD, USA, 1974; Volume 55.
4. Shen, W.C.; Smith, W.L.; Woolf, H. *An Intercomparison of Radiosonde and Satellite-Derived Cross Sections during the AMTEX*; Number 72; National Environmental Satellite Service: Silver Spring, MD, USA, 1975.
5. Horn, L.H.; Petersen, R.A.; Whittaker, T.M. Intercomparisons of data derived from Nimbus 5 temperature profiles, rawinsonde observations and initialized LFM model fields. *Mon. Weather. Rev.* **1976**, *104*, 1362–1371. [CrossRef]
6. Hilsenrath, E.; Coley, R.; Kirschner, P.; Gammill, B. *A Rocket Ozonesonde for Geophysical Research and Satellite Intercomparison*; Technical Report; NASA: Greenbelt, MD, USA, 1979.
7. Trenberth, K.; Jones, P.; Ambenje, P.; Bojariu, R.; Easterling, D.; Klein Tank, A.; Parker, D.; Rahimzadeh, F.; Renwick, J.; Rusticucci, M.; et al. Chapter 3. Observations: Surface and atmospheric climate change. In *Climate Change 2007. The Physical Science Basis. Contribution of Working Group I to the Fourth Assessment Report of the Intergovernmental Panel on Climate Change*; Solomon, S., Qin, D., Manning, M., Chen, Z., Marquis, M., Averyt, K.B., Tignor, M., Miller, H.L., Eds.; Cambridge University Press: Cambridge, UK, 2007; pp. 235–336.
8. Teunissen, P.; Montenbruck, O. *Springer Handbook of Global Navigation Satellite Systems*; Springer Handbooks; Springer International Publishing: Berlin/Heidelberg, Germany, 2017.
9. Foelsche, U.; Scherllin-Pirscher, B.; Ladstädter, F.; Steiner, A.; Kirchengast, G. Refractivity and temperature climate records from multiple radio occultation satellites consistent within 0.05%. *Atmos. Meas. Tech.* **2011**, *4*, 2007–2018. [CrossRef]
10. Anthes, R. Exploring Earth's atmosphere with radio occultation: Contributions to weather, climate and space weather. *Atmos. Meas. Tech.* **2011**, *4*, 1077–1103. [CrossRef]
11. Chen, D.; Rojas, M.; Samset, B.; Cobb, K.; Diongue Niang, A.; Edwards, P.; Emori, S.; Faria, S.; Hawkins, E.; Hope, P.; et al. Framing, context, and methods. *Clim. Chang.* **2021**, *478*, 147–286.
12. Zeng, Z.; Sokolovskiy, S.; Schreiner, W.S.; Hunt, D. Representation of vertical atmospheric structures by radio occultation observations in the upper troposphere and lower stratosphere: Comparison to high-resolution radiosonde profiles. *J. Atmos. Ocean. Technol.* **2019**, *36*, 655–670. [CrossRef]
13. Scherllin-Pirscher, B.; Steiner, A.K.; Kirchengast, G.; Schwärz, M.; Leroy, S.S. The power of vertical geolocation of atmospheric profiles from GNSS radio occultation. *J. Geophys. Res. Atmos.* **2017**, *122*, 1595–1616. [CrossRef]
14. Wilhelmsen, H.; Ladstädter, F.; Scherllin-Pirscher, B.; Steiner, A.K. Atmospheric QBO and ENSO indices with high vertical resolution from GNSS radio occultation temperature measurements. *Atmos. Meas. Tech.* **2018**, *11*, 1333–1346. [CrossRef]
15. Stocker, M.; Ladstädter, F.; Wilhelmsen, H.; Steiner, A.K. Quantifying Stratospheric Temperature Signals and Climate Imprints From Post-2000 Volcanic Eruptions. *Geophys. Res. Lett.* **2019**, *46*, 12486–12494. [CrossRef]
16. Chahine, M.T.; Pagano, T.S.; Aumann, H.H.; Atlas, R.; Barnet, C.; Blaisdell, J.; Chen, L.; Divakarla, M.; Fetzer, E.J.; Goldberg, M.; et al. AIRS: Improving weather forecasting and providing new data on greenhouse gases. *Bull. Am. Meteorol. Soc.* **2006**, *87*, 911–926. [CrossRef]

17. Hilton, F.; Atkinson, N.; English, S.; Eyre, J. Assimilation of IASI at the Met Office and assessment of its impact through observing system experiments. *Q. J. R. Meteorol. Soc. J. Atmos. Sci. Appl. Meteorol. Phys. Oceanogr.* **2009**, *135*, 495–505. [CrossRef]
18. Bouillon, M.; Safieddine, S.; Hadji-Lazaro, J.; Whitburn, S.; Clarisse, L.; Doutriaux-Boucher, M.; Coppens, D.; August, T.; Jacquette, E.; Clerbaux, C. Ten-year assessment of IASI radiance and temperature. *Remote Sens.* **2020**, *12*, 2393. [CrossRef]
19. Angerer, B.; Ladstädter, F.; Scherllin-Pirscher, B.; Schwärz, M.; Steiner, A.K.; Foelsche, U.; Kirchengast, G. Quality aspects of the Wegener Center multi-satellite GPS radio occultation record OPSv5. 6. *Atmos. Meas. Tech.* **2017**, *10*, 4845–4863. [CrossRef]
20. Gleisner, H.; Lauritsen, K.B.; Nielsen, J.K.; Syndergaard, S. Evaluation of the 15-year ROM SAF monthly mean GPS radio occultation climate data record. *Atmos. Meas. Tech.* **2020**, *13*, 3081–3098. [CrossRef]
21. Steiner, A.K.; Ladstädter, F.; Ao, C.O.; Gleisner, H.; Ho, S.P.; Hunt, D.; Schmidt, T.; Foelsche, U.; Kirchengast, G.; Kuo, Y.H.; et al. Consistency and structural uncertainty of multi-mission GPS radio occultation records. *Atmos. Meas. Tech.* **2020**, *13*, 2547–2575. [CrossRef]
22. Blackwell, W.; Milstein, A. A neural network retrieval technique for high-resolution profiling of cloudy atmospheres. *IEEE J. Sel. Top. Appl. Earth Obs. Remote Sens.* **2014**, *7*, 1260–1270. [CrossRef]
23. Susskind, J.; Blaisdell, J.M.; Iredell, L. Improved methodology for surface and atmospheric soundings, error estimates, and quality control procedures: The atmospheric infrared sounder science team version-6 retrieval algorithm. *J. Appl. Remote Sens.* **2014**, *8*, 84994. [CrossRef]
24. Hersbach, H.; Bell, B.; Berrisford, P.; Hirahara, S.; Horányi, A.; Muñoz-Sabater, J.; Nicolas, J.; Peubey, C.; Radu, R.; Schepers, D.; et al. The ERA5 global reanalysis. *Q. J. R. Meteorol. Soc.* **2020**, *146*, 1999–2049. [CrossRef]
25. Bell, B.; Hersbach, H.; Simmons, A.; Berrisford, P.; Dahlgren, P.; Horányi, A.; Muñoz-Sabater, J.; Nicolas, J.; Radu, R.; Schepers, D.; et al. The ERA5 global reanalysis: Preliminary extension to 1950. *Q. J. R. Meteorol. Soc.* **2021**, *147*, 4186–4227. [CrossRef]
26. Immler, F.; Dykema, J.; Gardiner, T.; Whiteman, D.; Thorne, P.; Vömel, H. Reference quality upper-air measurements: Guidance for developing GRUAN data products. *Atmos. Meas. Tech.* **2010**, *3*, 1217–1231. [CrossRef]
27. Mason, P.J.; Simmons, A.; Bojinski, S.; Mikalsen, A.C.; Richter, C.; Lindstrom, E.J.; Dolman, H.; Fischer, A.; Saunders, R.; Schulz, J.; et al. Systematic Observation Requirements for Satellite-Based Products for Climate Supplemental Details to the Satellite-Based Component of the Implementation Plan for the Global Observing System for Climate in Support of the UNFCCC (2010 Update), World Meteorological Organization, 2011; 138p. Available online https://library.wmo.int/viewer/48411/download?file=gcos-154.pdf&type=pdf (accessed on 21 September 2023).
28. Zemp, M.; Chao, Q.; Han Dolman, A.J.; Herold, M.; Krug, T.; Speich, S.; Suda, K.; Thorne, P.; Yu, W. GCOS 2022 Implementation Plan. In *Global Climate Observing System GCOS*; University of Zurich: Zurich, Switzerland, 2022; p. 85.
29. Rodgers, C.D. *Inverse Methods for Atmospheric Sounding: Theory and Practice*; World Scientific: Singapore, 2000; Volume 2.
30. Weaver, D.; Strong, K.; Schneider, M.; Rowe, P.M.; Sioris, C.; Walker, K.A.; Mariani, Z.; Uttal, T.; McElroy, C.T.; Vömel, H.; et al. Intercomparison of atmospheric water vapour measurements at a Canadian High Arctic site. *Atmos. Meas. Tech.* **2017**, *10*, 2851–2880. [CrossRef]
31. Tradowsky, J.S. Radiosonde Temperature Bias Corrections using Radio Occultation Bending Angles as Reference. 2017. Available online: https://rom-saf.eumetsat.int/Publications/reports/romsaf_vs31_rep_v11.pdf (accessed on 20 June 2023).
32. Gilpin, S.; Rieckh, T.; Anthes, R. Reducing representativeness and sampling errors in radio occultation–radiosonde comparisons. *Atmos. Meas. Tech.* **2018**, *11*, 2567–2582. [CrossRef]
33. Jing, X.; Shao, X.; Liu, T.C.; Zhang, B. Comparison of gruan rs92 and rs41 radiosonde temperature biases. *Atmosphere* **2021**, *12*, 857. [CrossRef]
34. Sun, B.; Reale, A.; Seidel, D.J.; Hunt, D.C. Comparing radiosonde and COSMIC atmospheric profile data to quantify differences among radiosonde types and the effects of imperfect collocation on comparison statistics. *J. Geophys. Res. Atmos.* **2010**, *115*. [CrossRef]
35. Sun, B.; Reale, T.; Schroeder, S.; Pettey, M.; Smith, R. On the accuracy of Vaisala RS41 versus RS92 upper-air temperature observations. *J. Atmos. Ocean. Technol.* **2019**, *36*, 635–653. [CrossRef]
36. Sun, B.; Calbet, X.; Reale, A.; Schroeder, S.; Bali, M.; Smith, R.; Pettey, M. Accuracy of Vaisala RS41 and RS92 upper tropospheric humidity compared to satellite hyperspectral infrared measurements. *Remote Sens.* **2021**, *13*, 173. [CrossRef]
37. Ho, S.p.; Peng, L.; Vömel, H. Characterization of the long-term radiosonde temperature biases in the upper troposphere and lower stratosphere using COSMIC and Metop-A/GRAS data from 2006 to 2014. *Atmos. Chem. Phys.* **2017**, *17*, 4493–4511. [CrossRef]
38. ROMSAF. Product Archive. 2017. Available online: https://rom-saf.eumetsat.int/product_archive.php (accessed on 19 June 2023).
39. Fassò, A.; Ignaccolo, R.; Madonna, F.; Demoz, B.; Franco-Villoria, M. Statistical modelling of collocation uncertainty in atmospheric thermodynamic profiles. *Atmos. Meas. Tech.* **2014**, *7*, 1803–1816. [CrossRef]
40. Virman, M.; Bister, M.; Räisänen, J.; Sinclair, V.A.; Järvinen, H. Radiosonde comparison of ERA5 and ERA-Interim reanalysis datasets over tropical oceans. *Tellus A Dyn. Meteorol. Oceanogr.* **2021**, *73*, 1–7. [CrossRef]
41. Hoffmann, L.; Spang, R. An assessment of tropopause characteristics of the ERA5 and ERA-Interim meteorological reanalyses. *Atmos. Chem. Phys.* **2022**, *22*, 4019–4046. [CrossRef]
42. Imfeld, N.; Haimberger, L.; Sterin, A.; Brugnara, Y.; Brönnimann, S. Intercomparisons, error assessments, and technical information on historical upper-air measurements. *Earth Syst. Sci. Data* **2021**, *13*, 2471–2485. [CrossRef]

43. Nash, J.; Oakley, T.; Vömel, H.; Wei, L. WMO Intercomparison of High Quality Radiosonde Systems (12 July–3 August 2010; Yangjiang, China). WMO Intercomparison of High Quality Radiosonde Systems. WMO/TD-No. 1580; IOM Report-NoWMO Geneve; 107; 2011. https://library.wmo.int/records/item/50499-wmo-intercomparison-of-high-quality-radiosonde-systems (accessed on 20 June 2023).
44. Navas-Guzmán, F.; Kämpfer, N.; Schranz, F.; Steinbrecht, W.; Haefele, A. Intercomparison of stratospheric temperature profiles from a ground-based microwave radiometer with other techniques. *Atmos. Chem. Phys.* **2017**, *17*, 14085–14104. [CrossRef]
45. Dirksen, R.J.; Sommer, M.; Immler, F.J.; Hurst, D.F.; Kivi, R.; Vömel, H. Reference quality upper-air measurements: GRUAN data processing for the Vaisala RS92 radiosonde. *Atmos. Meas. Tech.* **2014**, *7*, 4463–4490. [CrossRef]
46. Robert, H.; Shumway, D.S.S. *Time Series Analysis and Its Applications with R Examples*; Springer: Berlin/Heidelberg, Germany, 2017; Volume 1.
47. Fassò, A.; Sommer, M.; von Rohden, C. Interpolation uncertainty of atmospheric temperature profiles. *Atmos. Meas. Tech.* **2020**, *13*, 6445–6458. [CrossRef]
48. Colombo, P.; Fassò, A. Quantifying the interpolation uncertainty of radiosonde humidity profiles. *Meas. Sci. Technol.* **2022**, *33*, 74001. [CrossRef]
49. Sommer, M.; von Rohden, C.; Simeonov, T.; Oelsner, P.; Naebert, T.; Romanens, G.; Jauhiainen, H.; Survo, P.; Dirksen, R. *GRUAN Characterisation and Data Processing of the Vaisala RS41 Radiosonde*; GRUAN Technical Document 8; GRUAN Lead Center: Lindenberg, Germany, 2023. Available online: https://www.gruan.org/documentation/gruan/td/gruan-td-8 (accessed on 20 September 2023).
50. Survo, P.; Hiltunen, E.; Jauhiainen, H.; Lentonen, J.; Leppänen, J.; Salo, T.; Turunen, M. Atmospheric Temperature and Humidity Measurements of Vaisala Radiosonde RS41. In Proceedings of the WMO Technical Conference on Meteorological and Environmental Instruments and Methods of Observations, Saint Petersburg, Russian, 7–9 July 2014.
51. Huang, Y.; Zhang, Y.; Zhao, Y.; Chambers, J.A. A novel robust Gaussian–Student's t mixture distribution based Kalman filter. *IEEE Trans. Signal Process.* **2019**, *67*, 3606–3620. [CrossRef]